

# ARID ZONE JOURNAL OF ENGINEERING, TECHNOLOGY & ENVIRONMENT

AZOJETE December 2025. Vol.21(4):992-1004
Published by the Faculty of Engineering, University of Maiduguri, Maiduguri, Nigeria.

Print ISSN: 1596-2490, Electronic ISSN: 2545-5818
https://doi.org/10.63958/AZOJETE/2025/21/04/009

www.azojete.com.ng



#### **ORIGINAL RESEARCH ARTICLE**

# ANALYSIS OF THE PROPERTIES OF SPARK PLASMA SINTERED Ti6AI4V MATRIX COMPOSITES ENHANCED WITH NITRIDE NANOPARTICLES

J. O. Abe\* 1, 2, O. M. Popoola and A. P. I. Popoola

<sup>1</sup> Centre for Energy and Electric Power, Department of Electrical Engineering, Tshwane University of Technology, P.M.B. X680, Pretoria, South Africa.

<sup>2</sup> Department of Chemical, Metallurgical and Materials Engineering, Tshwane University of Technology, P.M.B. X680, Pretoria, South Africa.

\*Corresponding author's e-mail address: <u>johnabe.fm@gmail.com</u>

#### **ARTICLE INFORMATION**

### Received: 6<sup>th</sup> October 2025 Revised: 22<sup>nd</sup> November 2025 Accepted: 24<sup>th</sup> November 2025

# **Keywords:**

Ti6Al4V matrix composite
Refractory nitride
Spark plasma sintering
Microhardness
Potentiodynamic polarization

#### **ABSTRACT**

Ti6Al4V alloy serves as an optimal lightweight structural material. However, its restricted hardness adversely impacts its abrasion resistance under highperformance structural conditions, thereby hindering its extensive use in the aerospace industry. This study employed spark plasma sintering (SPS) to develop Ti6Al4V matrix composites reinforced with 1, 3, and 5 wt. % of three refractory nitride nanoparticles of h-BN, TiN, and AlN. The developed composites were analyzed for microstructure, phase composition, densification, microhardness, and potentiodynamic polarization using field-emission gun scanning electron microscopy, X-ray diffraction, the Archimedes' method, microindentation, and linear polarization investigations. The microstructure and phase analyses revealed marginal porosity and cracks, with no indications of detrimental intermetallic phases. It was observed that as reinforcement content increased, composite densities decreased from 98.4 to 97.4 %, 98.62 to 97.63 %, and 98.64 to 95.14 % for h-BN, TiN, AIN reinforcements, respectively. The microindentation test indicated that, relative to the unreinforced alloy (331.79 HV), hardness increased proportionally with reinforcement content. Interestingly, h-BN exhibits a range of 672.05 to 740.43 HV, TiN ranges from 427.18 to 491.06 HV, and AlN shows values from 441.25 to 504.68 HV. The composite with 3 wt. % AIN presented the best potentiodynamic polarization behaviour with a superior polarization resistance of 5246.2  $\Omega$  and a lowered corrosion rate of 0.14321 mm/year. Meanwhile, 5 wt. % AIN-reinforced composite showed the worst densification and potentiodynamic polarization behaviour with a relatively decreased polarization resistance of 219.13  $\Omega$  and a higher corrosion rate of 3.6935 mm/year. Additionally, among the developed composites, the 3 wt. % h-BN-reinforced composite exhibited optimal properties, showcasing a microhardness of 716.80 HV, a markedly improved polarisation resistance of 4011.2  $\Omega$ , and a considerably reduced corrosion rate of 0.21444 mm/year. Therefore, Improved mechanical and corrosion performance of Ti6Al4V matrix composites tends to reduce the weight of aerospace structures, improve fuel efficiency, and thereby enable the advancement of sustainable and benign aerospace technologies.

 $\hbox{@}$  2025 Faculty of Engineering, University of Maiduguri, Nigeria. All rights reserved.

#### I. Introduction

High-performance, lightweight materials have been intensively explored because the aerospace industries require durable, lightweight, fuel-efficient, and cost-effective materials (del Bosque et al., 2025). Titanium and its alloys are used in these industries due to their high specific strength, low specific gravity, and mechanical and corrosion resistance. More than half of titanium products are produced as Ti6Al4V alloy, which positions the alloy as the foundation of titanium alloys and aerospace manufacturing. However, the alloy's low hardness and inherently poor wear-resistant properties at ambient and heated temperatures limit its usage in structural

components (Garbiec et al., 2016). Moreover, materials deteriorate as a result of corrosion when they undergo chemical reactions with their environment. This phenomenon confronts several businesses, causing economic losses and safety risks (Aljibori et al., 2024). Maintaining aircraft component reliability and durability requires corrosion mitigation, preserving lives and resources (Thakur et al., 2025).

Quite a lot of approaches have been devised to address the highlighted problems (Garbiec et al., 2016). A considerable return on investment in avoiding costs can be achieved within the industry through the implementation of predictive maintenance and the investment in corrosion-resistant materials (Thakur et al., 2025). Alloying, surface changes, and reinforcing particle integration are often investigated (Ramesh et al., 2025). One approach that stands out is the development of Ti6Al4V matrix composites (TMCs) through reinforcing particle integration (Garbiec et al., 2016; Falodun et al., 2023). Refractory nitrides are suitable reinforcements for metal and alloy matrices due to their properties. Refractory nitrides are significant ceramics for high-temperature, structural, chemical, and semiconductor applications. This category contains silicon, boron, titanium, aluminium, niobium, tantalum, zirconium, and hafnium nitrides (Falodun et al., 2023; Abe et al., 2025). Because of their high melting point, hardness, thermal conductivity, high-temperature stability, chemical stability, and wear resistance, hexagonal boron nitride (h-BN), titanium nitride (TiN), and aluminium nitride (AlN) have received substantial research (Falodun et al., 2023; Abe et al., 2025; Hussain et al., 2022; Akinwamide et al., 2020).

Many studies have used refractory nitride as reinforcement materials, showing improvements in the developed composites' characteristics (Falodun et al., 2023; Abe et al., 2025; Hussain et al., 2022; Akinwamide et al., 2020; Liu et al., 2009). Hussain et al. (2022) used metal-organic chemical vapour deposition to synthesise a Cu-Ni composite reinforced with h-BN and examined its mechanical and thermal conductivity properties. Uniaxial tensile tests showed that h-BN improved composite mechanical properties over pure Cu-Ni alloy. The composite has 11.67%, 16.3%, and 27.9% higher ultimate tensile, yield, and fracture toughness. Threedimensionally interconnected h-BN layers at Cu-Ni grain boundaries improved composite characteristics. The layers make the composite load-resistant by grain refining, dislocation strengthening, and load transmission. Heat conductivity was 10% higher in the composite than in the pure Cu-Ni alloy. Akinwamide et al. (2020) examined the microstructural and corrosion characteristics of spark plasma sintering-produced TiN-modified 304 austenitic stainless steel in FeCl₃ and 3.5 wt. % NaCl. The Turbula mixing method produced uniform TiN dispersions in the austenitic stainless-steel matrix. After 96 hours in ferric chloride solution, 2 and 4 wt. % TiN specimens showed improved corrosion resistance. Cyclic potentiodynamic polarization experiments showed that TiN nanoparticles increased the sintered austenitic stainless steel pitting corrosion resistance. Lui et al. (2009) synthesised Al-AIN composites by arc plasma evaporating aluminium in nitrogen and hot pressing with AIN nanoparticle concentrations 0–39%. Microstructural examination indicates that nano AIN particles are uniformly dispersed within the Al nanocrystalline matrix, resulting in AlN/Al interfaces bonded atomically. The nanocomposites' hardness (3.48 GPa) and elastic modulus (142 GPa) were enhanced. The enhancement is attributable to the fortification caused by grain refinement and the interfacial bond formed at the solid Al/AIN interfaces.

There are a number of desired qualities associated with Ti6Al4V alloy as mentioned earlier; nevertheless, the production process is complicated by the alloy's strong affinity for nitrogen and oxygen. In order to get the desired results, the Ti6Al4V alloy needs to be processed under controlled circumstances, which include high temperatures and a vacuum (Garbiec et al., 2016). At elevated temperatures, conventional sintering methods present a number of challenges, including high melting points, lengthy dwell times, an inability to maintain low grain growth rates, large powder surface areas, and hazardous chemical affinities to atmospheric gases (hydrogen, nitrogen, and oxygen). As a result, a better approach is strongly recommended (Matizamhuka, 2016).

Spark plasma sintering is a sophisticated and effective process for sintering powder materials, enabling the production of near-net-shape bulk materials. This innovative consolidation technique functions through the concurrent application of pressure and rapid thermal treatment of powdered material. The parameters employed in the sintering procedure include low voltage and pressure, utilising a uniaxial force and pulsed direct current, respectively, to enhance the effectiveness of powder material sintering (Abe et al., 2025). The micro-spark/plasma theory is the predominant mechanism utilised to elucidate the SPS process, which relies on electrical arc discharge and the generation of plasma sparks at the powder particles interface. Various metallic and ceramic-based composite materials have been made using SPS and evaluated against traditional sintering methods. SPS features a short holding time and lower temperatures than traditional methods like casting or laser fusion, which results in reduced grain growth. Consequently, improved microstructural and mechanical qualities are achievable (Falodun et al., 2025).

Therefore, this work presents the manufacturing of Ti6Al4V matrix composites reinforced with I, 3, and 5 wt. % of h-BN, TiN, and AlN nanoparticles through the use of spark plasma sintering. The study is aimed at enhancing the microhardness and electrochemical corrosion resistance performance of spark plasma sintered TMCs, with the intention of utilizing them for structural applications in high-demand aerospace industries. This initiative aligns with Goal 9 of the Sustainable Development Goals (SDGs), which is to improve infrastructure and refit industries for sustainability with an emphasis on clean technology adoption and increased resource efficiency.

## 2. Materials and Methods

The starting powders for this work include a commercially pure Ti6Al4V alloy (>99% purity, average particle size 60µm, from TLS Technik, Germany) and refractory nitrides (h-BN, TiN, AlN) (average particle size 100nm, purity >99%) from Hongwu International Group Ltd., China. Three categories of Ti6Al4V-based powders with comparable weight compositions, along with a control sample were prepared, each with its corresponding code as follows: Ti6Al4V/1h-BN (TB1), Ti6Al4V/3h-BN (TB2), and Ti6Al4V/5h-BN (TB3); Ti6Al4V/1TiN (TT1), Ti6Al4V/3TiN (TT2), and Ti6Al4V/5TiN (TT3); Ti6Al4V/1AlN (TA1), Ti6Al4V/3AlN (TA2), and Ti6Al4V/5AlN (TA3); and Ti6Al4V alloy (T). The powders were measured using an electronic balance (Model EX10202, Canada) and mixed for 10 hours at 100 rpm in a turbula mixer.

The mixed powders were placed in a 30mm-diameter, 10mm-height cylindrical graphite die-punch assemblage in the sintering chamber. Based on an optimization experiment conducted by Abe et al., (2019), the consolidation of the powders was facilitated using an automatically operated SPS machine (model FCT Systeme GmbH, Germany) in a vacuum environment of approximately 4 Pa with optimized SPS parameters: 1000 °C, 30 MPa, 100 °C/min, and 10 min dwell time. A representation of the spark plasma sintering operation is shown in Figure 1. The sintered samples were wire-cut into  $10 \times 10 \times 5$  mm cuboids and hot-mounted in epoxy resin. The grinding process was accomplished utilizing European (P-Grade) silicon carbide abrasive sheets having grits in a range between P120 and P2400. DiaMaxx (9, 6, 3, and 1  $\mu$ ) was utilized to polish the samples to a mirror-like shine, followed by Kroll's reagent etching. The microstructure was examined under a field emission gun scanning electron microscope (FEGSEM: Zeiss 540 Ultra) with a high-magnification (Mag = 5.00 K) image and EDS, and the phases were identified using XRD Bruker D8 Advance.

An electronic density balance (SDPTOP JA5003J) was used to determine the sintered materials' density as prescribed in ASTM B962 and Archimedes' method. The relative densities were computed by dividing the densities measured by theoretical densities multiplied by 100%. The materials underwent microindentation utilizing an EMCO Vickers hardness tester that featured a diamond Dura scan. A 300gf test load was used to indent on the polished sample with 15 seconds dwell time at 0.5mm intervals. Five readings were averaged to calculate each sample's effective microhardness.

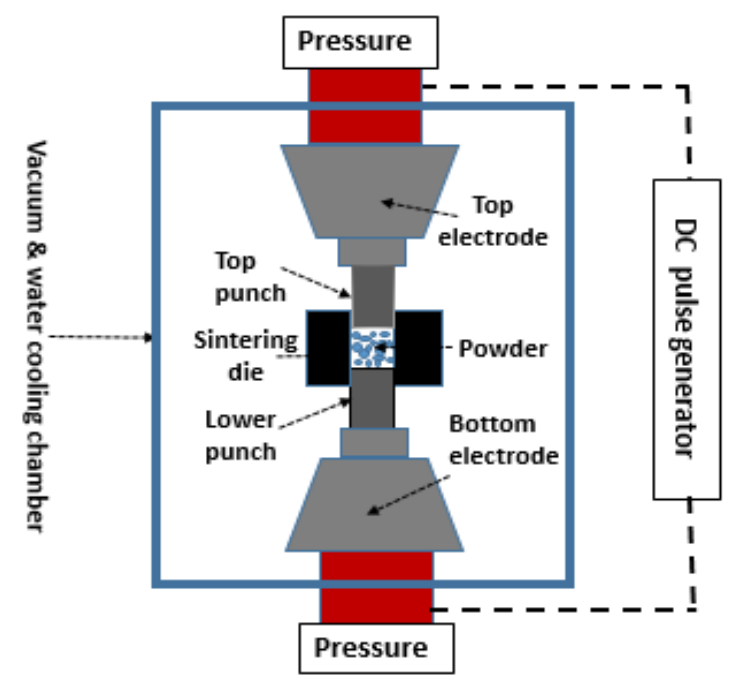


Figure 1: A representation of the spark plasma sintering operation

A linear polarization experiment was performed on a Metrohm Autolab Potentiostat (PGSTAT302N) with Nova software version 2.1.8 to evaluate the samples' potentiodynamic polarization behaviour in 0.5M sulphuric acid at ambient temperature. The scanning of the polarisation curves were conducted at a rate of 1 mV/s from 1.5 V to -1.5 V. An Ag/AgCl reference electrode contained in saturated KCl solution, a working electrode, and a platinum counter electrode were employed. The corrosion results were assessed using Tafel extrapolation.

#### 3. Results and Discussion

# 3.1. Microstructure and Phase Analyses of Ti6Al4V Matrix Composites

Plate I (a-d) displays the TEM images, while Figure 2(a-d) shows the stacked XRD patterns of the powders used for this study. Plate I (a) depicts spherical Ti6Al4V alloy particles, while Plate I (b-d) depicts platy-hexagonal h-BN, spherical TiN, and clumpy wurtzite-like AlN particles, respectively. On the other hand, Figure 2(a) shows the XRD pattern for Ti6Al4V alloy powder, revealing pristine  $\alpha$ -Ti phase peaks at diffraction angles of 35.09°, 38.42°, 40.17°, 53.0°, 62.95°, 70.66°, 76.22°, and 77.37° in the (100), (002), (101), (102), (110), (103), (112), and (201) planes. In Figure 2(b), crystalline hexagonal BN peaks have high intensity at 20 values of 26.63°, 41.51°, 43.75°, 50.0°, 54.85°, 75.73°, and 81.93°, aligning with planes (002, (100), (101), (102), (004), (110), and (105). This data describes hexagonal BN peaks with an average particle size of 100 nm from isothermal annealing (Abe et al., 2020). Figure 2(c) shows the crystalline TiN phase at  $2\theta = 36.66$ °, 42.6°, 61.81°, 74.07°, and 77.96°, corresponding to planes (111), (200), (220), (311), and (222). Furthermore, Figure 2(d) shows the presence of crystalline AlN phase peaks at  $2\theta = 33.22$ °, 36.04°, 37.92°, 49.82°, 59.35°, 66.05°, 69.73°, 71.44°, 72.63°, 76.45°, and 81.1°, in alignment with (100), (002), (101), (102), (110), (103), (200), (112), (201), (004), and (202) planes.

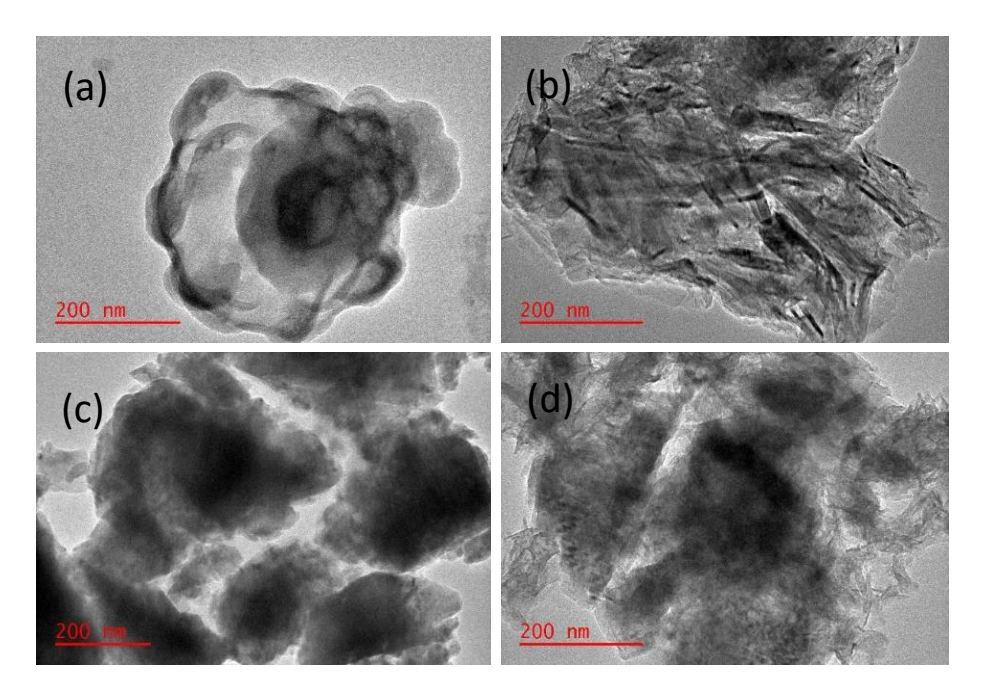


Plate I: TEM images of powders: (a) Ti6Al4V (b) h-BN (c) TiN (d) AlN

According to FEGSEM and standard EDS investigations, Plate 2 shows the structures and intensities of the peaks of the elemental constitution of T, TB1, TB2, TB3, TT1, TT2, TT3, TA1, TA2, and TA3. In Plate 2(ai), the T exhibits two phases ( $\alpha+\beta$ ). The phases exhibit diverse orientations, including ultrafine  $\alpha$  lamellae and bimodal configurations ( $\alpha$  lamellae and fine equiaxed grains), with a large presence of primary  $\alpha$  phases (Falodun et al., 2023). The EDS spectra in Plate 2(aii) indicate elemental peaks that match the expected values.

Plates 2(b), 2(c), and 2(d) indicate considerable morphological changes in the  $\alpha/\beta$  alloy matrix in contrast to T (Plate 2(ai)). The microstructure of reinforced composites varies due to h-BN, TiN, and AlN nanoparticles and increasing reinforcement levels from 1 to 5 wt. % (Abe et al., 2020). The EDS spectra in Plate 2(biv) confirm the presence of h-BN in the  $\alpha/\beta$  matrix by revealing elemental peaks for boron and nitrogen. The elemental peaks in Plate 2(civ) and Plate 2(div) show that TMCs reinforced with TiN (TT1, TT2 and TT3) and AlN (TA1, TA2 and TA3) include nitrides, mainly Ti, Al, and N.

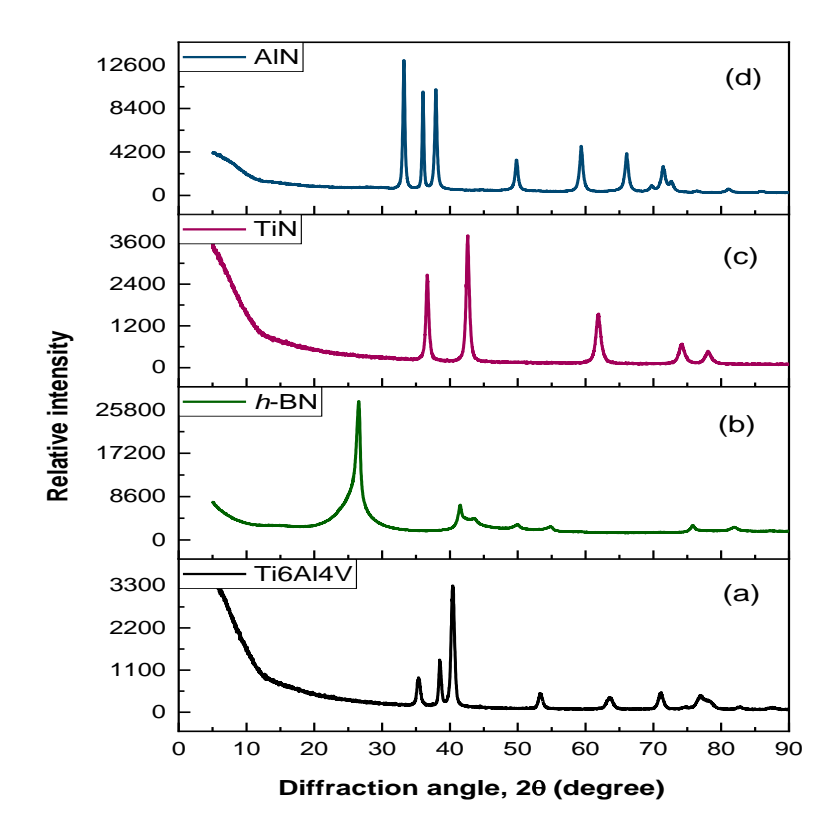


Figure 2: XRD patterns of the powders: (a) Ti6Al4V (b) h-BN (c) TiN and (d) AlN

Figure 3 compares the XRD images of T and the TMCs. In Figure 3, plot (a) clarifies  $\alpha$ -Ti and  $\beta$ -Ti phases in T (Falodun *et al.*, 2023). After mixing and dispersing the reinforcements in the alloy matrix, their XRD peak intensities decrease, also regarded as the broadening of the XRD peaks, indicating induced lattice strains due to the incidence of nanoscale crystals, as depicted in plots (b) to (g). This result is caused by the dilution of the reinforcement phase in the matrix, the refinement and dispersion of the reinforcement particles, potential interfacial interactions, and geometric reorganization that loses preferred orientation (Dudina *et al.*, 2021). Plots (b) and (c) show distinct XRD patterns that highlight the hard BN phase at  $2\theta \sim 44.3^{\circ}$  and the TiB phase at  $2\theta \sim 44.8^{\circ}$ . The peaks are necessary to understand the increased hardness and strength of *h*-BN-reinforced TMCs (TB1, TB2 and TB3) compared to TiN (TT1, TT2 and TT3) and AlN (TA1, TA2 and TA3) [32]. Plots (d), (e), (f), and (g) show that XRD peak intensities for  $\alpha$ -Ti ( $2\theta = 35.09^{\circ}$ ,  $40.17^{\circ}$ ,  $53.0^{\circ}$ ,  $62.95^{\circ}$ , and  $70.66^{\circ}$ ), VN ( $2\theta = 37.28^{\circ}$  and  $43.38^{\circ}$ ), and TiN ( $2\theta = 42.48^{\circ}$ ) are nearly identical in TiN- and AlN-reinforced TMCs.

The AIN phase is clearly visible at  $2\theta = 76.63^{\circ}$  in plots (d) and (e), whereas plots (f) and (g) show an additional TiN phase at  $2\theta = 78.08^{\circ}$ . This suggests that TiN- and AIN-reinforced TMCs share phase components and physical and chemical characteristics, which elucidates the similarity observed in their properties (Abe et al., 2020). None of the XRD patterns show deleterious intermetallic peaks. This shows that the refractory nitride reinforcements and Ti6Al4V matrix did not react negatively during SPS (Yang et al., 2025).

# 3.2. Density and Microhardness Analyses of Ti6Al4V Matrix Composites

The findings of the density and microhardness tests are presented in Table I. It is observed that T has a theoretical densification of 99.77%, which is quite close to full. This indicates that the SPS approach efficiently supports alloy consolidation by means of appropriate diffusional mass movement, which ultimately results in strong particle fusion, as seen by the FEGSEM image shown in Plate 2(ai). Relative densities are reduced when reinforcements of I, 3, and 5 weight percent h-BN, TiN, and AlN are added to T. The relative densities of TBI, TB2, and TB3 decrease from 98.40% to 97.40%, TTI, TT2, and TT3 decrease from 98.62% to 97.63%, and TAI, TA2, and TA3 decrease from 98.64% to 95.14%. The increased contact surface area explains this phenomenon due to the integration of nanoparticle reinforcements into the Ti6Al4V matrix, as well as pore nucleation at the locations of the ceramic particulates (Clinktan et al., 2019). The nature and proportion of reinforcement materials have a substantial impact on the densification characteristics of the TMCs (Irshad et al., 2023).

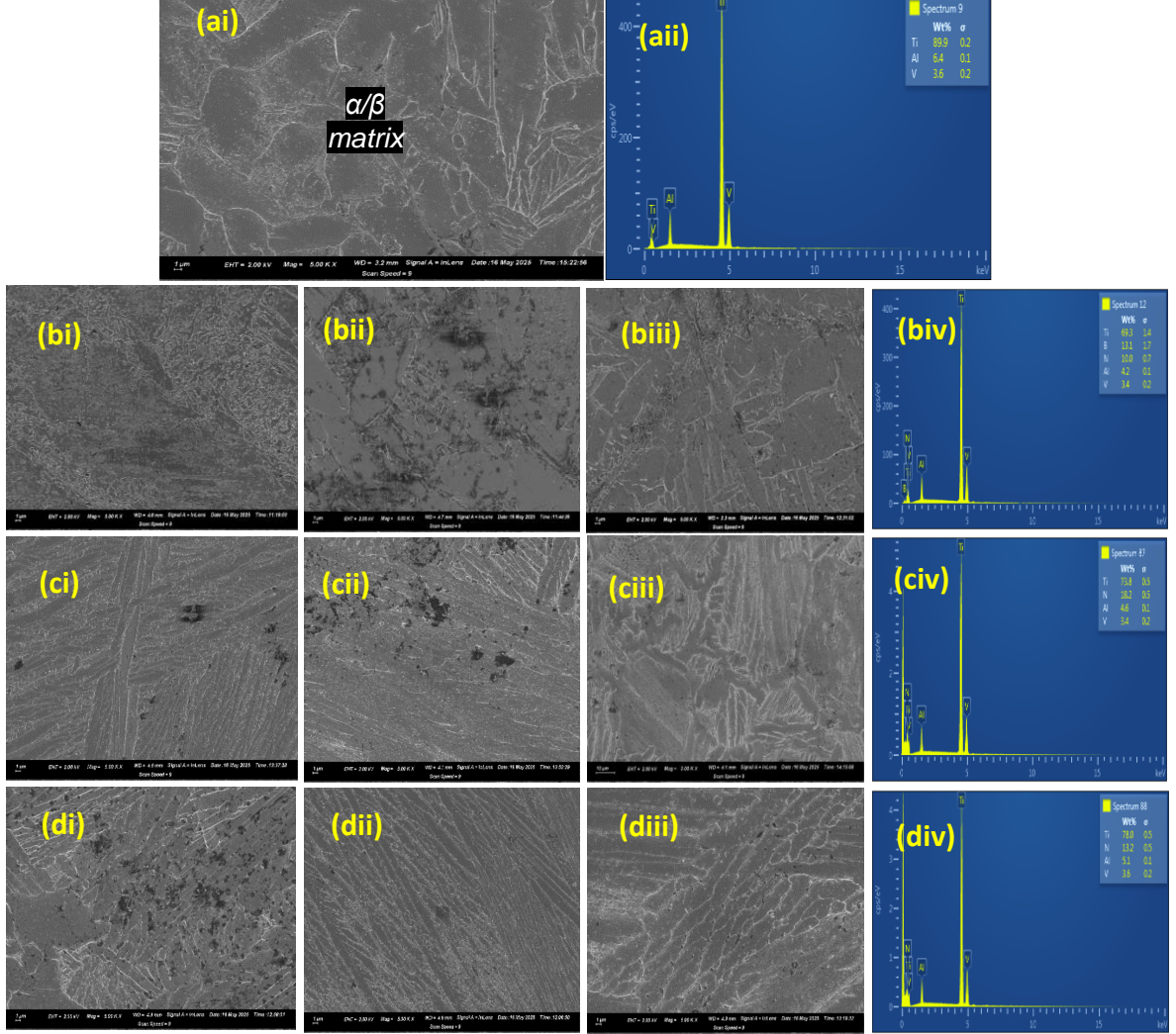


Plate 2: FEGSEM/EDS images depicting the structures and peaks of T (ai-aii), TB1, TB2 and TB3 (bi-biv), TT1, TT2 and TT3 (ci-civ), and TA1, TA2 and TA3 (di-div)

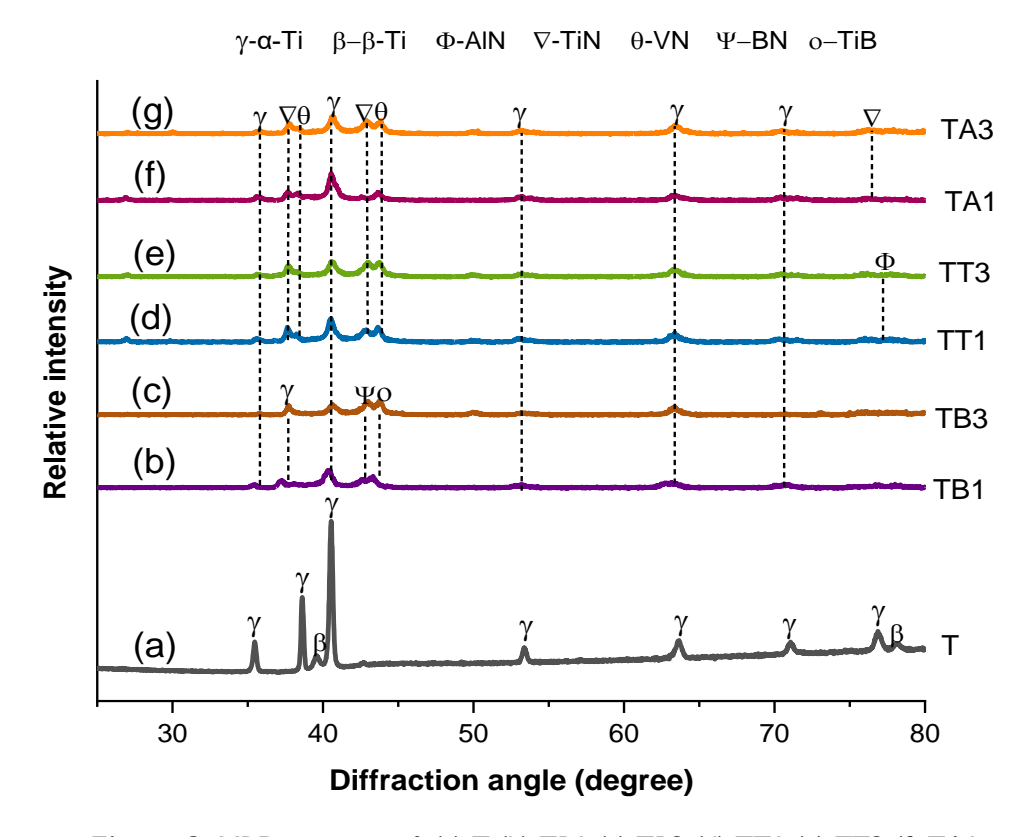
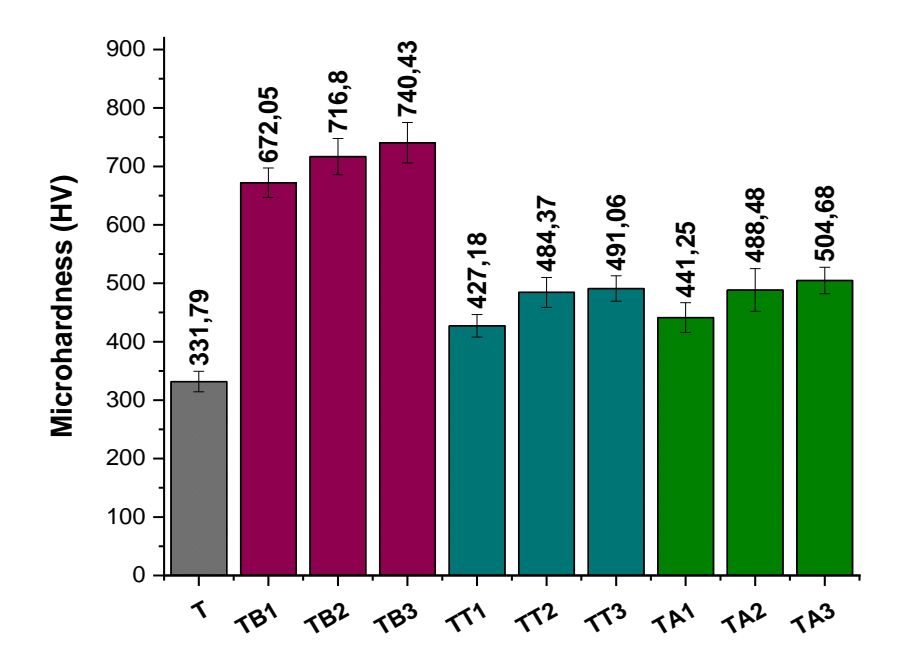


Figure 3: XRD patterns of: (a) T (b) TBI (c) TB3 (d) TTI (e) TT3 (f) TAI and (g) TA3

The evaluated average microhardness for T is 331.79HV, as illustrated in Figure 4. The most noticeable increase in microhardness is observed in TB1, TB2, and TB3, with values ranging from 672.05HV to 740.43HV. The two sets, which are TTI, TT2, and TT3, as well as TAI, TA2, and TA3, demonstrate comparable improvements in microhardness. The values for these sets range from 427.18HV to 491.06HV and from 441.25HV to 504.68HV, respectively. Thus, the microhardness of all the reinforced composites exhibits an increase with the concentration of ceramic reinforcement from I to 5 wt. %. This result can be attributed to the retention of BN, TiN, and AlN particles inside the  $\alpha/\beta$  matrix despite the fact that their densification dropped (Okoro et al., 2019). The retained particles are found to be uniformly dispersed, tightly bound, and distinct phases from the matrix. By effectively absorbing and distributing loads, these particles typically support the composite's strength, load-bearing capacity, and thereby improving hardness and wear resistance (Wang et al., 2025; Attar et al., 2014). Furthermore, during the sintering process, the ceramic reinforcement and titanium alloy undergo a reaction that results in the formation of harder phases (TiB and VN), which in turn increases the composite's hardness (Okoro et al., 2019). This discovery is in line with the findings of prior research Kganakga et al., (2020) that investigated the use of ceramic materials for the reinforcement of Ti6Al4V alloy. Thus, the microhardness of Ti6Al4V matrix composites can be increased by incorporating different types and proportions of nanoceramic reinforcements comprising h-BN, TiN, and AlN. This is achieved through the processes of dispersion strengthening and the pinning effect, which prevents dislocation movement (Okoro et al., 2019; Kganakga et al., 2020).

**Table 1:** Summary of the density and microhardness tests' results.

Sample ID code	Effective density (g/cm³)	Theoretical density (g/cm³)	Relative density (%)	Microhardness (HV)
Т	4.42	4.43	99.77	331.79 ± 17.6
TBI	4.31	4.38	98.40	672.05 ± 25.2
TB2	4.21	4.30	97.91	716.80 ± 31.0
TB3	4.12	4.23	97.40	740.43 ± 34.6
TTI	4.36	4.421	98.62	427.18 ± 19.3
TT2	4.33	4.423	97.90	448.37 ± 25.7
TT3	4.32	4.425	97.63	491.06 ± 21.8
TAI	4.34	4.40	98.64	441.25 ± 25.5
TA2	4.29	4.37	98.17	488.48 ± 36.5
TA3	4.13	4.34	95.14	504.68 ± 22.6



**Figure 4:** Graph comparing the microhardness of: (a) T (b) TB1 (c) TB2 (d) TB3 (e) TT1 (f) TT2 (g) TT3 (h) TA1 (i) TA2 and (j) TA3

# 3.3. Potentiodynamic Polarization Analysis of Ti6Al4V Matrix Composites

One of the techniques employed in preventing corrosion of materials is to develop new corrosion-resistant materials characterized by enhanced metallurgical structure that can provide resistance against the effect of corrosive anions (Chen et al., 2025). In this section, the potentiodynamic polarization approach is utilized to investigate the electrochemical corrosion of T, TBI, TB2, TB3, TTI, TT2, TT3, TAI, TA2, and TA3 in sulphuric acid at a concentration of 0.5 M. Table 2 provides a comprehensive overview of the extrapolated Tafel data obtained from the experiment. It highlights the essential corrosion parameters, such as the corrosion potential, current density, polarization resistance, corrosion rate, and the anodic and cathodic Tafel slopes ( $\beta$ a and  $\beta$ c). A comparison of the corrosion rates and polarization resistances of the materials is presented in Figure 5, while the potentiodynamic polarization curves of the materials are displayed in Figure 6. According to the data obtained from the potentiodynamic polarization investigation in Table 2, the inclusion of nitride nanoparticles has a multifarious impact on the electrochemical performance of the pure alloy. It is observed that T demonstrates a positive corrosion potential (-0.45687V) and a current density that is quite mild (5.6906x10- $\beta$ A/cm²) in comparison to other materials. This can be attributed to the effect of stable passivating films of titania, TiO2, and alumina, Al2O3, formed during the interactive activities between the Al and Ti elemental compositions in the alloy and the corrosive environment (Mogoda et al., 2004).

For the h-BN-reinforced composites, improvement in the electrochemical characteristics can be observed where the initial corrosion potential of T shifts from -0.45687V to a more positive value of -0.41961V with a corresponding decrease in current density from 5.69x10-5A/cm<sup>2</sup> to 1.04x10-5A/cm<sup>2</sup> as depicted by TB1. Increased polarization resistance and decreased corrosion rate resulted, rising from 897.69 $\Omega$  to 3864.7 $\Omega$  and decreasing from 1.8499mm/year to 0.2908mm/year, respectively. Further improvement in the electrochemical characteristics was observed in TB2, where corrosion potential rises to -0.40575V and current density decreases to 9.72x10-6A/cm<sup>2</sup>, resulting in increased polarization resistance and better corrosion rate of  $4011.2\Omega$  and 0.21444mm/year, respectively. On the other hand, it is found that TB3 displayed slightly worse electrochemical characteristics than TB2, but it still outperforms T and TB1. This may be due to more unfavourable interfacial interactions between the nitride reinforcement and alloy matrix phases, which could lead to corrosion-prone regions, as previously reported by Nsiah-Baafi et al., (2022). Similarly, the TiNreinforced composites (TTI, TT2, and TT3) show improved electrochemical characteristics, exhibiting a relatively improved polarization resistance that falls within the range of 2051.9 to 2908.6  $\Omega$  and an enhanced corrosion rate that falls within the range of 0.37174 to 0.29414 mm/year. This is characterized by less positive corrosion potential between -0.41561 and -0.37781V and reduced current density between 2.52x10-5A/cm<sup>2</sup> and I.08xI0-5A/cm<sup>2</sup> in contrast to T.

For AIN-reinforced TMCs, there is a notable increase in electrochemical characteristics from TAI to TA2, but there is characteristics with additional reinforcement at TA3, which is even worse than T and every other composite. Categorically, TA3 had the most unsatisfactory electrochemical performance, as evidenced by its corrosion potential of -0.46064V and current density of 2.56x10-4A/cm<sup>2</sup>. This led to a fall in polarization resistance and a rise in corrosion rate of 219.13Ω and 3.6935mm/year. The result is likely due to detrimental modifications in the surface condition of TA3 and inhomogeneous oxide layers formed during sintering. Pores observed in the composite could act as potential nucleation sites for corrosion processes, and localized pitting ensued due to particle agglomeration (Abe et al., 2020). This occurs despite the samples undergoing identical procedures, and it is common for the reinforcement to show greater corrosion resistance in diluted acid solution (Mogoda et al., 2004). Nevertheless, the porous oxide has the potential to create a channel for the electrolyte, which would make it easier for redox processes to take place (Xie et al., 2025). With a corrosion potential of -0.33065V and a current density of 4.83x10-6A/cm<sup>2</sup>, TA2 exhibited exceptional corrosion resistance qualities. This resulted in a rise in polarization resistance and a drop in corrosion rate, which was measured at  $5246.2\Omega$  and 0.14321mm/year, respectively. This is attributed to effective material densification and the formation of a homogenous oxide, which decreased the amount of contact between the electrolyte and the composite (Flores-Álvarez et al., 2017).

Table 3 presents a comparative analysis of the compositions and examined properties of the spark plasma sintered Ti6Al4V matrix composites from the current study alongside analogous materials documented in existing literature. The integration of diverse ceramic reinforcements has been observed to enhance the characteristics of Ti6Al4V-based composite systems, leading to notable advancements in mechanical and electrochemical properties as evinced by the studies examined. Of the presently developed materials, the composite reinforced with 3 wt. % h-BN is identified with the optimal properties as it demonstrates superior characteristics, attaining a microhardness of 716.80 HV, in addition to a markedly improved polarization resistance of 4011.2  $\Omega$  and a considerably reduced corrosion rate of 0.21444 mm/year.

**Table 2**: Summary of the potentiodynamic polarization test results.

Sample ID code	Corrosion potential,	Corrosion density, j <sub>corr</sub>	Corrosion rate	Polarization	βa (V/dec)	βc (V/dec)
ib code	E <sub>corr</sub> (V)	(A/cm <sup>2</sup> )	(mm/year)	resistance $(\Omega)$		
T	-0.45687	5.69×10 <sup>-5</sup>	1.8499	897.69	0.23772	0.26607
TBI	-0.41961	1.04×10 <sup>-5</sup>	0.2908	3864.7	0.11882	0.092793
TB2	-0.40575	9.72×10 <sup>-6</sup>	0.21444	4011.2	0.20293	0.15248
TB3	-0.43478	1.51×10 <sup>-5</sup>	0.63731	1538	0.28198	0.16794
TTI	-0.41561	2.52×10 <sup>-5</sup>	0.33991	2771.9	0.18821	0.10897
TT2	-0.37781	1.12×10 <sup>-5</sup>	0.29414	2908.6	0.25567	0.10563
TT3	-0.4076 I	1.08×10 <sup>-5</sup>	0.37174	2051.9	0.07368	0.12195
TAI	-0.36826	2.58×10 <sup>-5</sup>	0.56962	1612.9	0.14294	0.092555
TA2	-0.33065	4.83×10 <sup>-6</sup>	0.14321	5246.2	0.070161	0.11103
TA3	-0.46064	2.56×10 <sup>-4</sup>	3.6935	219.13	0.31277	0.34694

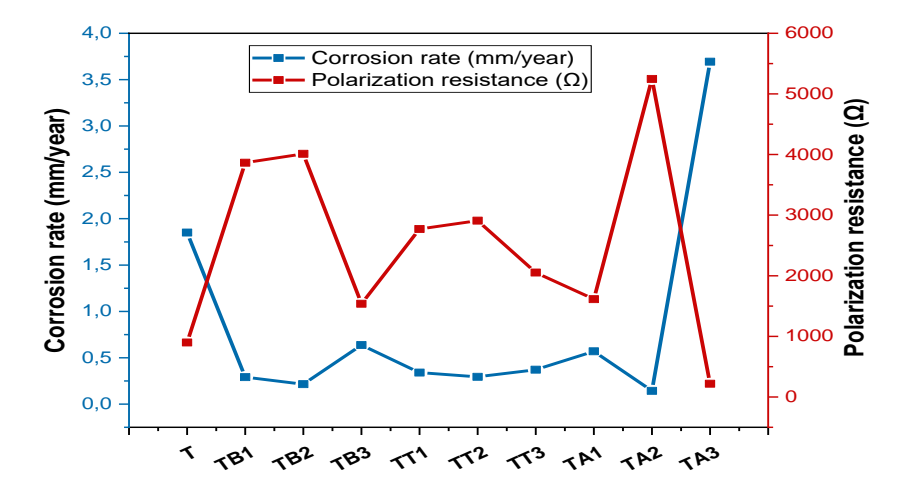
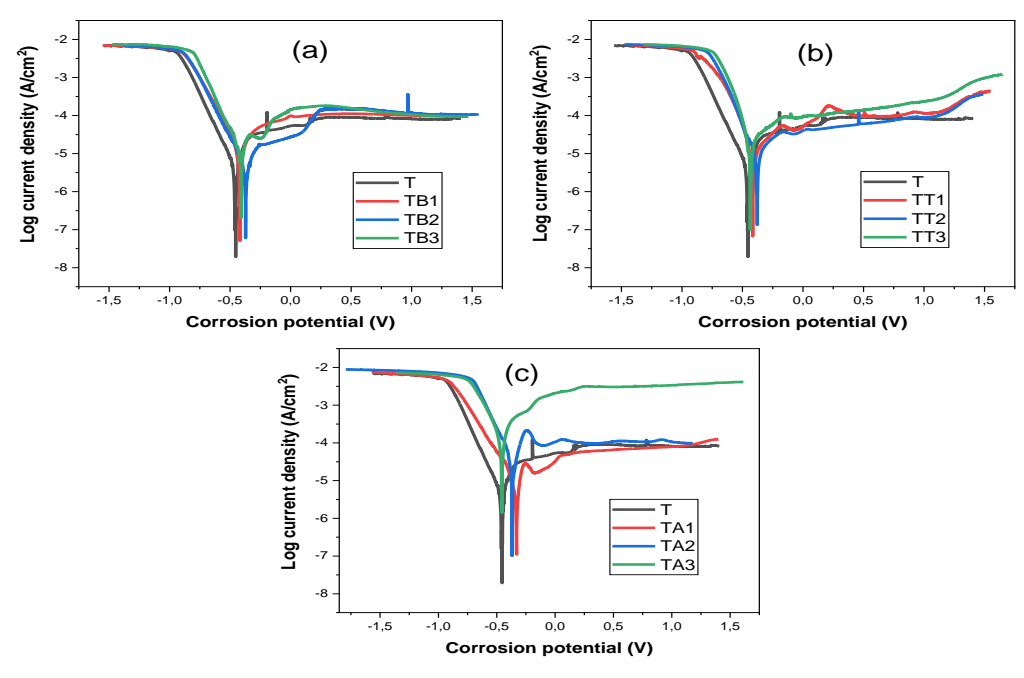


Figure 5: Graph comparing the corrosion rate and polarization resistance of: (a) T (b) TB1 (c) TB2 (d) TB3 (e) TT1 (f) TT2 (g) TT3 (h) TA1 (i) TA2 and (j) TA3



**Figure 6:** Plots comparing the potentiodynamic polarization curves for: (a) T, TB1, TB2 and TB3 (d) T, TT1, TT2 and TT3, and (f) T, TA1, TA2 and TA3

Table 3: Comparison among the properties of various spark plasma sintered Ti6Al4V matrix composites

-	9 1 1	Density, hardness, and corrosion properties				
Sintered sample	Spark plasma sintering conditions	Relative Microhardness density (%) (HV)		Corrosion rate (mm/yr)	Reference	
Ti6Al4V	1000 °C, 50 MPa, 100 °C/min, 6 min	98.6	325.46	0.986625	(Kgoete et al., 2018a)	
Ti6Al4V/5Si <sub>3</sub> N <sub>4</sub>		96.9	597.58	0.08234		
Ti6Al4V/10Si <sub>3</sub> N <sub>4</sub>		97.2	668.56	0.030547		
Ti6Al4V/15Si <sub>3</sub> N <sub>4</sub>		96.2	585.73	0.0671		
Ti6Al4V	900 °C, 50 MPa, 100 °C/min, 10 min	99.32	369	-	(Okoro et al., 2019)	
Ti6Al4V/0.5MWCNT		98.6	458.5	-		
Ti6Al4V/1.0MWCNT		98.2	466.5	-		
Ti6Al4V/1.5MWCNT		97.54	502.6	-		
Ti6Al4V	1000 °C, 50 MPa, 100 °C/min, 6 min	98.6	325.46	0.986625	(Kgoete et al., 2018b)	
Ti6Al4V/5TiN	, ,	98.3	527.43	0.14313	,	
Ti6Al4V/10TiN		97. I	438.8	0.243512		
Ti6Al4V/15TiN		96.2	487.68	0.275244		
Ti6Al4V	850 °C, 50 MPa, 100 °C/min, 5 min	-	374.6	0.0404	(Nsiah-Baafi et al., 2022)	
Ti6Al4V/3Al <sub>3</sub> O <sub>4</sub>	, -	-	395. I	0.0150	,	
Ti6Al4V/5Al <sub>3</sub> O <sub>4</sub>		-	406.5	0.0693		
Ti6Al4V/10Al <sub>3</sub> O <sub>4</sub>		-	424. I	0.0982		
Ti6Al4V	1000 °C, 50 MPa, 100 °C/min, 6 min	98.6	325.46	0.986625	(Kgoete et al., 2018c)	
Ti6Al4V/2.5Si₃N₄ +2.5TiN	, ,	98.4	603.39	0.19709	,	
Ti6Al4V/5Si <sub>3</sub> N <sub>4</sub> +5TiN		97.2	727.41	0.018		
Ti6Al4V/7.5Si₃N₄ +7.5TiN		96.5	708.7	0.379055		
Ti6Al4V	1000 °C, 30 MPa, 100 °C/min, 10 min	99.77	331.79	1.8499	Present study	
Ti6Al4V/1h-BN		98.40	672.05	0.2908		
Ti6Al4V/3h-BN		97.91	716.80	0.21444		
Ti6Al4V/5h-BN		97.40	740.43	0.63731		
Ti6Al4V/ITiN		98.62	427.18	0.33991		
Ti6Al4V/3TiN		97.90	448.37	0.29414		
Ti6Al4V/5TiN		97.63	491.06	0.37174		
Ti6Al4V/IAIN		98.64	441.25	0.56962		
Ti6Al4V/3AIN		98.17	488.48	0.14321		
Ti6Al4V/5AlN		95.14	504.68	3.6935		

#### 4. Conclusion

Spark plasma-sintered TMCs with I, 3, and 5 wt. % h-BN, TiN, and AlN nanoparticles were examined for microstructure, phase composition, density, microhardness, and potentiodynamic polarization. Finally, these are concluded:

- i. The study discovered that SPS processing decreases surface reactions and produces finely refined grains with strong bonds and high densification. Incorporating varying amounts of h-BN, TiN, and AlN (1, 3, and 5 wt. %) into the Ti6Al4V matrix results in a decrease in relative densities: 98.4% to 97.4% for h-BN-reinforced, 98.62% to 97.63% for TiN-reinforced, and 98.64% to 95.14% for AlN-reinforced composites.
- ii. Compared to the unreinforced alloy (331.79HV), the composites' hardness increases with reinforcement content from 1 to 5 wt. %: 672.05HV to 740.43HV, 427.18HV to 491.06HV, and 441.25HV to 504.68HV for h-BN, TiN, AIN reinforcements, respectively. The composites possess higher microhardness due to load transfer from the matrix to the more resilient reinforcement particles, which strengthens dispersion and inhibits dislocation motion. The microindentation test indicated that, relative to the unreinforced alloy (331.79 HV), hardness increased proportionally with reinforcement content.
- iii. In 0.5M sulphuric acid, 3 wt. % AIN resists corrosion best with a comparatively high polarization resistance (5246.2Ω) and low corrosion rate (0.14321mm/year). On the other hand, the composite with 5 wt. %

- AlN-reinforced composite with poor densification had the worst electrochemical characteristics in the same media, resulting in decreased polarization resistance and increased corrosion rate of  $219.13\Omega$  and 3.6935mm/year, respectively. Porous oxide could establish a pathway for the electrolyte to facilitate redox reactions, and localized pitting ensued due to particle agglomeration.
- iv. Among the spark plasma sintered composites, the 3 wt. % h-BN-reinforced composite exhibited optimal properties, achieving a microhardness of 716.80 HV, alongside a significantly enhanced polarisation resistance of 4011.2  $\Omega$  and a notably diminished corrosion rate of 0.21444 mm/year.
- v. The effectual development of Ti6Al4V matrix composites with improved microhardness and electrochemical corrosion behaviour is expected to alleviate Ti6Al4V alloy's aerospace structural applications, lessen weight in aerospace structures, and better fuel efficiency and emissions, and thereby enable the advancement of sustainable and benign aerospace technologies. Thus, this project aligns with Goal 9 of the Sustainable Development Goals (SDGs), which is to improve infrastructure and refit industries for sustainability with an emphasis on clean technology adoption and increased resource efficiency.

# **Acknowledgments**

This work is based on the research supported wholly/in part by the National Research Foundation of South Africa (Grant No. 150574), Centre for Energy and Electric Power (CEEP); Surface Engineering Research Laboratory (SERL) under the Leadership of Professor API Popoola, Faculty of Engineering and the Built Engineering in Tshwane University of Technology (TUT), Pretoria, South Africa.

#### References

Abe, JO., Popoola, API. and Popoola, OM. 2020. Consolidation of Ti6Al4V Alloy and Refractory Nitride Nanoparticles by Spark Plasma Sintering Method: Microstructure, Mechanical, Corrosion and Oxidation Characteristics. Materials Science and Engineering: A, 774:138920.

Abe, JO., Popoola, OM. and Popoola, API.. 2025. A Review of the Spark Plasma Sintering, Characterization, and Properties of Refractory Nitride-Reinforced Titanium-Based Composites. Nigerian Journal of Technological Development, 22(2):1-25.

Abe, JO., Popoola, OM., Popoola, API., Ajenifuja, E. and Adebiyi, DI. 2019. Application of Taguchi Design Method for Optimization of Spark Plasma Sintering Process Parameters for Ti-6Al-4V/h-BN Binary Composite. Engineering Research Express, I (2):025043.

Akinwamide, SO., Obadele, BA., Adams, FV. and Olubambi, PA. 2020. Microstructure and Corrosion Response of Spark-Plasma-Sintered 304 Austenitic Stainless Steel Reinforced with Titanium Nitride in Chloride Environments. Journal of Failure Analysis and Prevention, 20:833-842.

Aljibori, H., Al-Amiery, A. and Isahak, W.N.R. 2024. Advancements in corrosion prevention techniques. Journal of Bio-and Tribo-Corrosion, 10(4):78.

Attar, H., Bönisch, M., Calin, M., Zhang, LC., Scudino, S. and Eckert, J. 2014. Selective laser melting of in situ titanium—titanium boride composites: Processing, microstructure and mechanical properties. Acta Materialia, 76:13-22.

Chen, Y., He, Z., Li, H., Lu, D., Song, Y., Zhan, L., Pan, S. and Liu, W. 2025. Corrosion fatigue mechanisms and control technologies in aviation aluminium alloys: A critical review. Chinese Journal of Aeronautics, 103496.

Clinktan, R., Senthil, V., Ramkumar, KR., Sivasankaran, S. and Al-Mufadi, FA. 2019. Effect of Boron Carbide Nano Particles in CuSi4Zn14 Silicone Bronze Nanocomposites on Matrix Powder Surface Morphology and Structural Evolution Via Mechanical Alloying. Ceramics International, 45(3):3492-3501.

del Bosque, A., Vergara, D. and Fernández-Arias, P. 2025. An overview of smart composites for the aerospace sector. Applied Sciences, 15(6):2986.

Dudina, DV., Vidyuk, TM. and Korchagin, MA. 2021. Synthesis of ceramic reinforcements in metallic matrices during spark plasma sintering: Consideration of reactant/matrix mutual chemistry. Ceramics, 4(4):592-599.

Falodun, O., Akinwamide, O., Oke, S. and Bodunrin, M. 2025. Microstructural Characterization of Ceramic-Reinforced Ti–6Al–4V Alloys using SEM, EDS Mapping, and EBSD Techniques. Metallography, Microstructure, and Analysis, I-14.

Falodun, OE., Oke, SR., Akinwamide, SO., Ajibola, OO., Adebayo, AO., Borisade, SG., Adediran, AA. and Olubambi, PA. 2023. The effect of TiN-TiB<sub>2</sub> on the microstructure, wear, and nanoindentation behavior of Ti6Al4V-Ni-Cr matrix composites. Journal of Materials Engineering and Performance, 32(12):5566-5575.

Flores-Álvarez, JF., Rodríguez-Gómez, FJ., Onofre-Bustamante, E. and Genescá-Llongueras, J. 2017. Study of the Electrochemical Behaviour of a Ti6Al4V Alloy Modified by Heat Treatments and Chemical Conversion. Surface and Coatings Technology, 315:498-508.

Garbiec, D., Siwak, P. and Mróz, A. 2016. Effect of compaction pressure and heating rate on microstructure and mechanical properties of spark plasma sintered Ti6Al4V alloy. Archives of Civil and Mechanical Engineering, 16:702-707.

Hussain, Z., Jang, H., Choi, H. and Choi, BS. 2022. Microstructure, mechanical behavior, and thermal conductivity of three-dimensionally interconnected hexagonal boron nitride-reinforced Cu-Ni composite. Journal of Materials Engineering and Performance, 1-9.

Irshad, HM., Farooq, A., Hakeem, AS., Azeem, MZ. and Ehsan, MA. 2023. Electrochemical study of aluminum—cubic boron nitride composites synthesized via spark plasma sintering for engineering applications. Journal of Alloys and Compounds, 965:171210.

Kganakga, MG., Prieto, G., Falodun, OE., Tuckart, WR., Obadele, BA., Ajibola, OO. and Olubambi, PA. 2020. Erosion wear behavior of spark plasma-sintered Ti-6Al-4V reinforced with TiN nanoparticles. The International Journal of Advanced Manufacturing Technology, 110:3051-3060.

Kgoete, FM., Popoola, API. and Fayomi, OSI. 2018. Influence of spark plasma sintering on microstructure and corrosion behaviour of Ti-6Al-4V alloy reinforced with micron-sized Si3N4 powder. Defence Technology, 14(5), 403-407.

Kgoete, FM., Popoola, API. and Fayomi, OSI. 2018. Data on the influence of TiN on wear and corrosion behavior of Ti–6Al–4V alloy fabricated through spark plasma sintering. Data in brief, 19, 1989.

Kgoete, FM., Popoola, API., Fayomi, OSI., and Adebiyi, ID. 2018. Spark plasma sintered Ti-6Al-4V-Si3N4-TiN ternary composites: Effect of combined microsized Si3N4 and TiN addition on microstructure and mechanical properties for aerospace application. Journal of Alloys and Compounds, 769, 817-823.

Liu, YQ., Cong, HT., Wang, W., Sun, CH. and Cheng, HM. 2009. AlN nanoparticle-reinforced nanocrystalline Al matrix composites: Fabrication and mechanical properties. Materials Science and Engineering: A, 505(1-2):151-156.

Matizamhuka, WR. 2016. Spark Plasma Sintering (SPS) - An Advanced Sintering Technique for Structural Nanocomposite Materials. Journal of the Southern African Institute of Mining and Metallurgy: 116(12):1171-1180.

Mogoda, AS., Ahmad, YH. and Badawy, WA. 2004. Corrosion Behaviour of Ti6Al4V Alloy in Concentrated Hydrochloric and Sulphuric Acids. Journal of Applied Electrochemistry, 34:873-878.

Nsiah-Baafi, E., Andrews, A., Diouf, S. and Olubambi, PA. 2022. Wear and Corrosion Properties of Spark Plasma Sintered Ti6Al4V–Al2O3 Composites. Open Ceramics, 10:100260.

Okoro, AM., Machaka, R., Lephuthing, SS., Oke, SR., Awotunde, MA. and Olubambi, PA. 2019. Evaluation of the sinterability, densification behaviour and microhardness of spark plasma sintered multiwall carbon nanotubes reinforced Ti6Al4V nanocomposites. Ceramics International, 45(16):19864-19878.

Ramesh, S., Kudva, SA., Gurumurthy, BM., Kumar, P., Kumar, S., Prashanth, BM., Adiga, S., Anne, G. and Karthik, BM. 2025. Development of Mg-Zn-Mn Surface Composites Reinforced with ZnO Through Friction

Stir Processing and Investigation of Corrosion and Wear Behavior. Journal of Bio-and Tribo-Corrosion, 11(2):48.

Thakur, A., Kaur, H., Anadebe, VC., Purohit, S. and Kumar, A. 2025. Corrosion in the Aerospace Industry. Industrial Corrosion: Fundamentals, Failure, Analysis and Prevention, 217-254.

Wang, Y., Yang, G., Zhang, S., Zhou, S., Li, B., An, D., He, B., Li, X., Xiao, Y. and Lin, P. 2025. Microstructure evolution and mechanical properties of in-situ Ti6Al4V–TiB-Ti2Ni composites manufactured by laser directed energy deposition. Composites Part B: Engineering, 292:112072.

Xie, Y., Dong, J., Wu, L., Wang, W., Sun, X., Meng, X. and Huang, Y. 2025. Unraveling the relationship between severe plastic deformation and corrosion responses of AZ31 Mg alloys. Corrosion Science, 250, 112881.

Yang, G., Zhang, S., Zhou, S., Li, B., An, D., He, B., Li, X., Xiao, Y. and Lin, P. 2025. Microstructure evolution and mechanical properties of in-situ Ti6Al4V–TiB-Ti2Ni composites manufactured by laser directed energy deposition. Composites Part B: Engineering, 292:112072.